Anisotropic absorption and emission of bulk $(1\bar{1}00)$ AlN

Martin Feneberg* and María Fátima Romero
Institut für Experimentelle Physik, Otto-von-Guericke-Universität Magdeburg, Universitätsplatz 2, 39106 Magdeburg, Germany

Marcus Röppischer, Christoph Cobet, and Norbert Esser
Leibniz-Institut für Analytische Wissenschaften–ISAS–e.V., Albert-Einstein-Strasse 9, 12489 Berlin, Germany

Benjamin Neuschl and Klaus Thonke
Institut für Quantenmaterie/Gruppe Halbleiterphysik, Universität Ulm, 89069 Ulm, Germany

Matthias Bickermann†
Department Werkstoffwissenschaften, Materialien für die Elektronik und Energietechnologie, Friedrich-Alexander-Universität Erlangen-Nürnberg, Martensstrasse 7, 91058 Erlangen, Germany

Rüdiger Goldhahn
Institut für Experimentelle Physik, Otto-von-Guericke-Universität Magdeburg, Universitätsplatz 2, 39106 Magdeburg, Germany

(Received 6 February 2013; revised manuscript received 19 April 2013; published 24 June 2013)

The intrinsic anisotropic optical properties of wurtzite AlN are investigated in absorption and emission. Full access to the anisotropy of the optical response of the hexagonal material is obtained by investigating the $(1\bar{1}00)$ plane of a high-quality bulk crystal allowing electric field **E** polarization perpendicular ($\mathbf{E} \perp \mathbf{c}$) and parallel ($\mathbf{E} \parallel \mathbf{c}$) to the optical axis **c**. Spectroscopic ellipsometry yields the ordinary ($\varepsilon_\perp$) and extraordinary ($\varepsilon_\parallel$) dielectric functions (DFs) from 0.58 up to 20 eV. The comparison of the experimental data with recently calculated DFs demonstrates that Coulomb interaction has a strong impact not only on the spectral dependence around the fundamental absorption edge but also on the high-energy features usually discussed in terms of van Hove singularities. The fits of the second-order derivatives of $\varepsilon_\parallel$ and $\varepsilon_\perp$ provide the transition energies for the main features in this range. The DFs close to the fundamental absorption edge, dominated by free excitons, exciton-phonon complexes, and the exciton continuum, are independently confirmed by reflectivity and synchrotron-based photoluminescence excitation studies. Values for the band gaps, the crystal field ($\Delta_{cf} = -221 \pm 2$ meV), and spin-orbit splittings ($\Delta_{so} = 13 \pm 2$ meV) are obtained. Furthermore, we obtain accurate values for the static dielectric constants of $\varepsilon_{S\perp} = 7.65$ and $\varepsilon_{S\parallel} = 9.21$, entering, e.g., the calculations of exciton binding energies. Photoluminescence is used to investigate the emission properties of the same sample.

DOI: 10.1103/PhysRevB.87.235209 PACS number(s): 71.35.−y, 77.22.Ch

I. INTRODUCTION

Ongoing interest in wurtzite aluminum nitride (AlN) has triggered lots of studies dealing with the optical properties of this highest-band-gap wurtzite III–nitride semiconductor material. Similar to the case of gallium nitride (GaN), AlN is already used in demonstrator devices[1] despite the fact that its optical properties are neither understood nor documented sufficiently.

Furthermore, AlN is believed to have a high technological potential as a substrate material for short-wavelength emitters, as the high-band-gap material is transparent up to about 200 nm[2,3] and allows for low-strain active regions composed of high-aluminum-content AlGaN.[4–7] These applications in turn triggered improvements in the growth of high-quality AlN,[8–10] only recently allowing us to investigate the fundamental properties of this semiconductor in unpreceded quality. For example, the full width at half maximum of donor bound-exciton recombinations in AlN could be shown to be below 500 μeV, allowing for unambiguous identification of these lines,[11,12] or the optical properties of nonpolar quantum wells in AlN barriers could be understood.[13]

The behavior around the fundamental band gap is strongly influenced by the valence band (VB) order at the Γ point of the Brillouin zone (BZ). It is now generally accepted that AlN exhibits a negative crystal-field energy Δ_{cf} of about −220 meV but a positive spin-orbit energy Δ_{so} of about 11–22 meV (a sampling of experimental and theoretical data is provided below). As a consequence, one finds an uppermost VB with Γ^v_{7+} symmetry and two lower remote bands with Γ^v_9 and Γ^v_{7-} symmetry. Optical transitions between these states and the Γ^c_7 conduction band (CB) are usually labeled as A ($\Gamma^v_{7+} \leftrightarrow \Gamma^c_7$), B ($\Gamma^v_9 \leftrightarrow \Gamma^c_7$), and C ($\Gamma^v_{7-} \leftrightarrow \Gamma^c_7$). The transition probability for A is weak for light with the polarization of the electric field vector perpendicular to the **c** axis ($\mathbf{E} \perp \mathbf{c}$) but high for the parallel polarization ($\mathbf{E} \parallel \mathbf{c}$). The opposite applies for C, while B is strictly forbidden for $\mathbf{E} \parallel \mathbf{c}$ and thus is only observable for $\mathbf{E} \perp \mathbf{c}$.

Typical high-quality AlN samples are heteroepitaxially grown layers with the polar **c** (0001) orientation. The common experimental setup ($\mathbf{E} \perp \mathbf{c}$) allows access to the higher-energy transitions related to Γ^v_9 and Γ^v_{7-}. Only in luminescence, population arguments and possibly large acceptance angles lead to observable contributions related to Γ^v_{7+}. The fine

structure of the free excitons related to the A transition has been reported recently.[14] In this work, a further splitting into excitons of Γ_5 and Γ_1 symmetries has been observed. Modeling yielded a negative spin-exchange interaction constant of $j = -4$ meV. However, in absorption and reflectance studies large angles of incidence have to be used in order to enhance the sensitivity for A (part of the light is then polarized parallel to **c**). In particular, the analysis of spectroscopic ellipsometry (SE) spectra provides the ordinary $\bar{\varepsilon}_\perp$ and the extraordinary $\bar{\varepsilon}_\parallel$ dielectric functions (DF) corresponding to $\mathbf{E} \perp \mathbf{c}$ and $\mathbf{E} \parallel \mathbf{c}$, respectively.[15,16] However, SE of (0001)-oriented films does not allow us to determine the anisotropy far above the band gap.

In the framework of density functional theory, wurtzite AlN is a frequently investigated prototype semiconductor.[17,18] Its large band gap and the spread of characteristic absorption features over a wide frequency range make it especially appropriate to demonstrate the influence of exchange correlation[19–21] on the quasiparticle band structure and to evaluate the suitability/accuracy of different approaches for obtaining the correct atomic geometry in the ground state and the band structure accounting for the excitation of electrons or holes. In order to allow comparison with measured optical spectra, the electron-hole interaction has to be taken into account in the final step. This excitonic DF is obtained via solving the Bethe-Salpeter equation using the quasiparticle wave functions. The inclusion of excitonic effects causes a pronounced redistribution of oscillator strength and a redshift of the absorption features with respect to the so-called van Hove singularities (critical points) in the quasiparticle band structure. Although AlN has been studied by different computational approaches in the past,[22,23] experimental data of the anisotropic dielectric functions are still missing. As demonstrated previously for InN[24] and GaN,[25] the accurate determination of $\bar{\varepsilon}_\perp$ and $\bar{\varepsilon}_\parallel$ in the high-energy range requires high-quality $(1\bar{1}00)$ or $(11\bar{2}0)$ surfaces. The preparation of these facets became only recently possible with the availability of large enough boules of single-crystalline bulk AlN. In contrast to heteroepitaxial films, strain has almost no influence on the characteristic transition energies for samples prepared from bulk material.

This paper is organized as follows. In Sec. II, we briefly describe the sample properties and specify the experimental setups. In Sec. III, the experimental results are presented, discussed, and compared to theoretical expectations. This contains the anisotropic DF from 0.58 to 20 eV, an assignment of high-energy critical points, the dispersion of ε_1 in the transparency region, the DF around the band gap, and related emission properties. Finally, a short summary is given in Sec. IV.

II. EXPERIMENT

The bulk AlN crystal under study, the same crystal used in Ref. 14, was grown by physical vapor transport at about 2000 °C. It was cut from the boule and wafered by standard techniques to a thickness of about 500 μm. The surface normal is $[1\bar{1}00] \pm 0.3°$, as confirmed by Laue diffraction. Lattice constants of $c = 4.9810$ Å and $a = 3.1109$ Å were obtained by high-resolution x-ray diffraction. Earlier studies confirmed high transmissivity at ultraviolet wavelengths (between $\lambda =$ 220 and 380 nm) of more than 25% corresponding to $\alpha \leqslant 13\ \mathrm{cm}^{-1}$.[2] A detailed chemical analysis of a companion sample yielded impurity concentrations of $[\mathrm{O}] = 7 \times 10^{18}\ \mathrm{cm}^{-3}$, $[\mathrm{Si}] = 5 \times 10^{18}\ \mathrm{cm}^{-3}$, and $[\mathrm{C}] = 6 \times 10^{17}\ \mathrm{cm}^{-3}$.

Photoluminescence was excited by ArF* excimer laser pulses with $\lambda = 193$ nm ($E = 6.42$ eV). The light source for reflectivity spectra was a D_2 lamp. A spectral resolution of 250 μeV at 6 eV was achieved. For studies under variable temperature, the sample was placed in a cryostat cooled by liquid helium. All optical parts such as windows, lenses, polarizers, and mirrors are specially selected for suitability in the ultraviolet spectral range. A commercial rotating analyzer ellipsometer was employed for the spectroscopic ellipsometry (SE) studies in the photon energy range from 0.58 to 6.4 eV. Here, the ellipsometric parameters Ψ and Δ were recorded at room temperature for angles of incidence of 60°, 67°, and 74°. SE in the range from 5 to 20 eV was performed by using the ellipsometer[25] attached to the Berlin electron storage ring for synchrotron radiation (BESSY II). At this setup, the angle of incidence was 67.5° for energies up to 10 eV and 45° for shorter wavelengths. For the spectra spanning a high-energy range, the spectral resolution decreases from 3 meV (at 5 eV) to 12 meV (at 20 eV). Using the synchrotron ellipsometer, the insertion of a cold-finger cryostat allowed temperature-dependent measurements between $T = 10$ and 295 K around the fundamental absorption edge. For these studies, the spectral resolution was enhanced to 1 meV.

In order to get access to both the ordinary and the extraordinary dielectric tensor components, the sample was measured in two configurations for which the **c** axis is oriented either parallel or perpendicular to the plane of incidence. The complex DFs ($\bar{\varepsilon}_\gamma = \varepsilon_{1\gamma} + j\varepsilon_{2\gamma}$, $\gamma = \perp, \parallel$) were obtained by fitting Ψ and Δ in a multilayer model,[26] which also takes into account the 1-nm root-mean-square surface roughness (from atomic force microscopy) via effective medium approximation.[26]

Additionally, the Superlumi station at beamline I of the DORIS III synchrotron at DESY, Hamburg (Germany), was employed to record photoluminescence excitation (PLE) spectra and reflectivity under inclined incidence of light at $T =$ 10 K.[27]

III. RESULTS AND DISCUSSION

A. High-energy features of the anisotropic dielectric function

Figures 1(a) and 1(b) show a comparison of the real and imaginary parts of the complex DFs as obtained for wurtzite AlN, respectively. Here, the full energy range from 0.58 to 20 eV is shown at $T = 295$ K. Obviously, both parts of the DF exhibit a strong anisotropy. Peaks and intensities of ε_1 and ε_2 vary characteristically between the ordinary ($\mathbf{E} \perp \mathbf{c}$) and extraordinary ($\mathbf{E} \parallel \mathbf{c}$) DFs. In order to demonstrate the similarities to wurtzite GaN, the corresponding results of $\varepsilon_{2\perp}$ and $\varepsilon_{2\parallel}$ from Refs. 25 and 28 are shown in Fig. 1(c).

To further discuss the origin of the features we focus on ε_2 only because they are mirrored in ε_1 due to the Kramers-Kronig relation. Ordinary and extraordinary ε_2 are characterized by a sharp onset of absorption at the band gap of wurtzite AlN

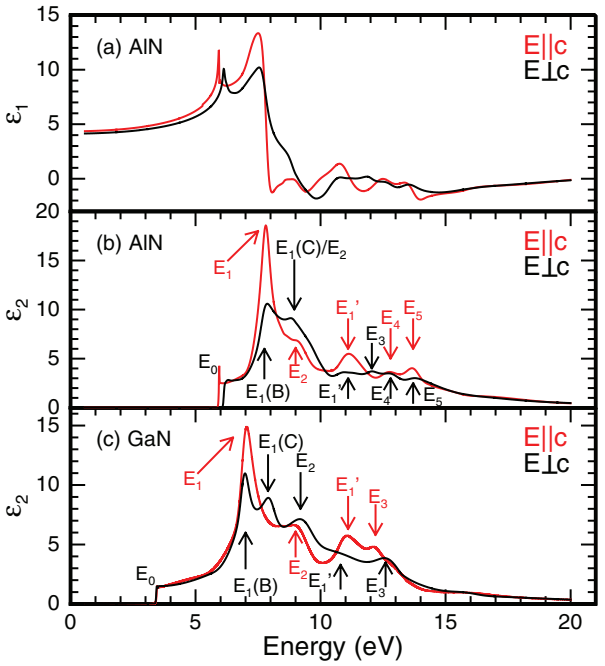

FIG. 1. (Color online) Experimental (a) real and (b) imaginary parts of the ordinary ($\mathbf{E} \perp \mathbf{c}$, black) and extraordinary ($\mathbf{E} \parallel \mathbf{c}$, red) dielectric functions of wurtzite AlN at room temperature in an energy range from 0.58 to 20 eV. The labels are explained in the text; corresponding energy values are summarized in Table I. (c) The imaginary parts of the ordinary (black) and extraordinary (red) dielectric functions of wurtzite GaN are shown in the same energy range for comparison, composed from Refs. 25 and 28.

(≈6 eV), labeled E_0. This will be discussed in more detail in Sec. III C. The higher-energy features can partly be identified in analogy to wurtzite GaN,[25] for which the imaginary parts of the DF are presented in Fig. 1(c). The absorption contributions there are labeled following Ref. 25. By comparing the general line shape of the extraordinary ε_2 of GaN and AlN, we can identify peaks E_1, E_2, and E_1'.

Now we compare the ordinary ε_2 of AlN with the extraordinary one. At approximately the same energy position where E_1 was found for $\mathbf{E} \parallel \mathbf{c}$, $E_1(B)$ is found for $\mathbf{E} \perp \mathbf{c}$, similar to GaN. The contributions labeled $E_1(C)$ and E_2 are well separable in GaN but seem to overlap as a broad shoulder in AlN. However, E_1' can again be found in ε_2 for both materials as it is a prominent contribution in the extraordinary DF and appears at a similar energy position in the ordinary one but with lower amplitude.

Features even higher in energy cannot be identified so far; we therefore label them in increasing energy order both for GaN and AlN. It should be mentioned that the peak named E_3 in GaN is not necessarily identical to the one labeled E_3 in AlN. On the contrary, we suspect E_3 in GaN to be analogous to E_5 in AlN, as can be seen from the DFs of AlGaN thin films (not shown here).

Figure 2 additionally presents spectra of ε_2 calculated theoretically by density functional theory including quasiparticle corrections and excitonic coupling between electrons and holes.[22,23] The good agreement between the shown calculation and our experiment allows us to transfer assignments already

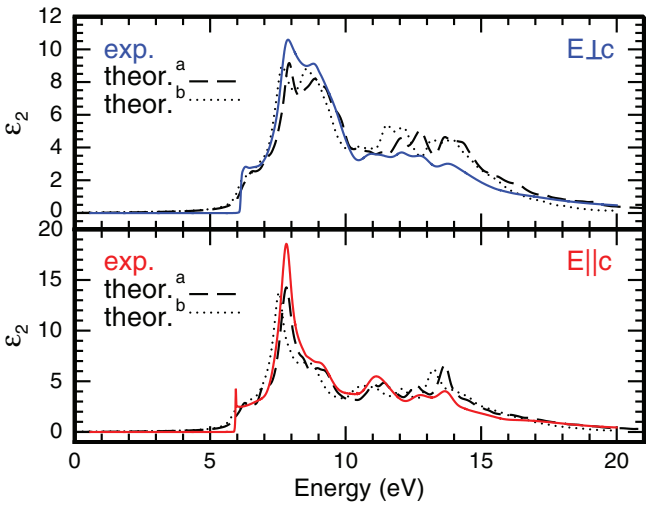

FIG. 2. (Color online) Comparison of experimental (blue and red) and calculated (black) imaginary parts of the dielectric functions. The top graph shows the ordinary part, and the lower one shows the extraordinary part. Theoretical results are taken from (a) Ref. 22 and (b) Ref. 23.

drawn in Ref. 22 to our case. The E_1 and $E_1(B)$ transitions are assigned to absorption along the U line (i.e., the connection line between M and L points) in the BZ. E_2 and $E_1(C)$ are probably related to K- and M-point interband transitions appearing at similar energies. Also higher CB absorption at the Γ point can contribute, especially for $\mathbf{E} \parallel \mathbf{c}$. The E_1' feature can stem from absorption around the K point.

However, it should be kept in mind that a band structure, even already including quasiparticle corrections, cannot be used easily for a one-by-one assignment of energy values because the excitonic or Coulomb interaction changes the shape of the DF considerably.[22] Such high-energy excitonic effects can be of the order of eV, prohibiting the classical approach, where structures in the DF are considered as directly linked to critical points of the band structure.[29]

For quantitative analysis of the energy values of high-energy features in ε, we calculated the second derivative of the point-by-point DF after surface correction multiplied by the square of the photon energy.[30] The resulting traces can be fitted[31] by

$$\frac{d^2}{d(\hbar\omega)^2}[(\hbar\omega)^2\bar{\varepsilon}] = \sum_j \frac{A_j e^{i\Phi_j}}{(\hbar\omega - E_j + i\Gamma_j)^3}, \qquad (1)$$

with Φ_j, A_j, Γ_j, and E_j being the phase angle, amplitude, broadening factor, and transition energy of the jth transition, respectively. The exponent in the denominator is fixed to 3 because strong Coulomb interaction leads to transitions which are, even at high-energy critical points, exciton-like, as discussed above. Due to the Kramers-Kronig consistency of the DFs, the real and imaginary parts of Eq. (1) yield the same parameters when applied to ε_1 and ε_2, respectively. In Fig. 3, for example, the second derivatives and the corresponding fits to the extraordinary DF are shown. The overall agreements of fits and experimental traces for the whole energy range are obvious. The energy values E_j obtained are summarized in Table I. Close inspection of Fig. 3 indicates that around

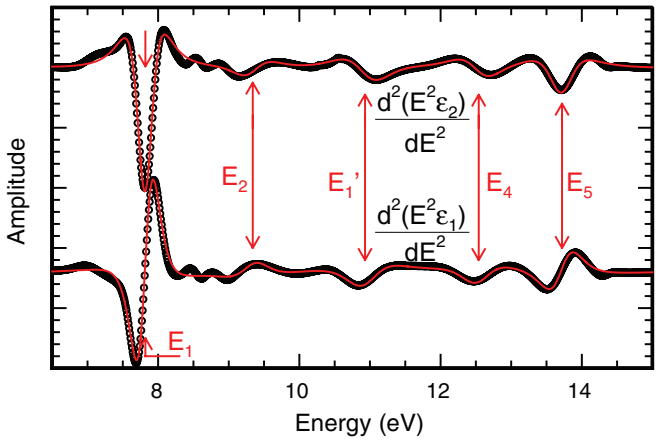

FIG. 3. (Color online) Second derivative of the extraordinary dielectric function multiplied by the square of the photon energy (symbols), together with the according fits (solid lines) to evaluate transition energies with high accuracy.

7–7.5 eV and around 8.5–9 eV oscillations are visible in the second derivative of the real and imaginary parts. They are eventually related to further transition energies which must be clarified with future experiments on additional samples.

B. High-frequency and static dielectric constants

The knowledge of the high-frequency (ε_∞)[32] and static (ε_S) dielectric constants is crucial for correctly analyzing the screening effects in any semiconductor as they enter into the calculation of, e.g., exciton binding energies.[33,34] To obtain quantitative results for ε_∞, the low-energy part of ε_1 in the transparent region of AlN has to be analyzed, i.e., where ε_2 is zero. In this energy range, ε_1 equals the square of the refractive index. Notably, the dispersion of ε_1 for both polarization directions of the electric field is governed by the oscillator structure at ≈7.8 eV, where maxima labeled E_1 and E_1(B) in ε_2 show up. Because of the anisotropy of the energy position and amplitude of E_1 and E_1(B), the dispersion of ε_1 in the visible range is anisotropic as well. It can be modeled by the empirical equation[35]

$$\varepsilon_1(\hbar\omega) = 1 + \frac{2}{\pi}\left(\frac{A_G}{2}\ln\frac{E_H^2-(\hbar\omega)^2}{E_G^2-(\hbar\omega)^2} + \frac{A_H E_H}{E_H^2-(\hbar\omega)^2}\right). \quad (2)$$

TABLE I. Energy positions and tentative assignments of prominent high-energy features of the dielectric functions at $T = 295$ K. The labels appear again in Figs. 1 and 3. Possible origins of the absorption bands in the Brillouin zone (BZ) are also given, as explained in the text. The accuracy for all values is ±10 meV.

E ⊥ c			**E ∥ c**		
	(eV)	BZ		(eV)	BZ
E_1(B)	7.72	$M-L$	E_1	7.82	$M-L$
E_1(C)/E_2	8.83	M/K	E_2	9.34	Γ
E_1'	10.45	K	E_1'	10.93	K
E_3	11.98				
E_4	12.80		E_4	12.54	
E_5	13.52		E_5	13.72	

TABLE II. Parameter sets for the empirical description of ε_1 below the fundamental band gap at $T = 295$ K. The high-frequency dielectric constants ε_∞ calculated as asymptotic value for $\hbar\omega \to 0$ in Eq. (2) and the static dielectric constants are also given.

	E_G (eV)	E_H (eV)	A_G	A_H (eV)	ε_∞	ε_S
E ⊥ c	6.19	10.71	4.2	28.3	4.14 ± 0.02	7.65
E ∥ c	5.94	9.70	3.8	32.8	4.34 ± 0.02	9.21

Here, E_G represents an effective value for the band gap energy, and E_H is an energy value representing the averaged contribution from high-energy critical points. A_G and A_H are the corresponding amplitude factors, respectively. Fitting Eq. (2) to both traces of ε_1 below the fundamental band gap yields the parameter sets summarized in Table II. There, the high-frequency dielectric constants ε_∞ are also given as derived from the $\hbar\omega \to 0$ limit of Eq. (2).

Using the Lyddane-Sachs-Teller[36] relation $\varepsilon_S = (\omega_{LO}/\omega_{TO})^2\varepsilon_\infty$ and the optical phonon frequencies at room temperature from Ref. 37, we can calculate the static dielectric constants. By using $\omega_{LO\parallel} = 890\ \mathrm{cm}^{-1}$ and $\omega_{TO\parallel} = 611\ \mathrm{cm}^{-1}$ for the infrared-allowed A_1 modes, we obtain $\varepsilon_{S\parallel} = 9.21$. For the other polarization direction, the E_1(LO) and E_1(TO) frequencies of $\omega_{LO\perp} = 912\ \mathrm{cm}^{-1}$ and $\omega_{TO\perp} = 670.8\ \mathrm{cm}^{-1}$, respectively, result in $\varepsilon_{S\perp} = 7.65$. The ratio $\varepsilon_{S\perp}/\varepsilon_{S\parallel}$ is 0.831, which is only slightly lower than estimated earlier.[38] The geometric mean value $\varepsilon_S = \sqrt{\varepsilon_{S\perp}\varepsilon_{S\parallel}} = 8.39$ is frequently used as an estimate of an isotropic equivalent for the static dielectric constant.

C. Dielectric function around the band gap

Wurtzite AlN is characterized by a large negative crystal-field energy $\Delta_{cf} = (-221 \pm 2)$ meV and a small positive spin-orbit splitting $\Delta_{so} = (13 \pm 2)$ meV. These values result from the low-temperature results of this study; an overview of previously published values is summarized in Table III. Electron-hole interaction leads to the formation of excitons with the binding energy of 55 meV or slightly smaller[55,56] for the A exciton, while the binding energies for B and C excitons were found to be similar.[16]

We performed SE experiments at different temperatures between $T = 10$ and 295 K. The dependence of the anisotropic ε_2 spectra around the band gap is presented in Fig. 4. Besides the redshift with increased temperature, the evolution of increasing broadening and thus damping can be observed easily.

The anisotropic absorption behavior of wurtzite AlN around the band gap results from the concurrence of several processes, all linked to excitonic resonances. Again, it can be discussed best by means of the imaginary part of the DF, ε_2. In Fig. 5 details of ε_2 in both orientations for the electric field vector are shown as measured at $T = 10$ K. The onsets of the experimental curves show a large energy distance, as expected. For **E** ∥ **c** this onset is only slightly above 6 eV, while for **E** ⊥ **c** this position is about 200 meV higher in energy, mirroring the distance between the excitons formed with a hole from the topmost Γ_{7+} VB and holes from the combined lower VBs, respectively. A detailed line

TABLE III. Crystal field Δ_{cf} and spin-orbit splitting Δ_{so} as reported in the literature compared to our results. The respective method used together with the sample orientation/structure are additionally noted; however, they are given for various temperatures. The references are ordered chronologically. OR means optical reflection, CL is cathodoluminescence, PL is photoluminescence, and SE stands for spectroscopic ellipsometry.

	Δ_{cf} (meV)	Δ_{so} (meV)	Technique	Sample
Ref. 39	−200		Theory	
Ref. 40	−58.5	20.4	Theory	
Ref. 41	−217	19	Theory	
Ref. 42	−215	19	Theory	
Ref. 43	−176		Theory	
Ref. 44	−169	11	Theory	
Ref. 45	−244		Theory	
Ref. 46	−219		Theory	
Ref. 47	−224	19	Theory	
Ref. 48	−275.8	21.8	Theory	
Ref. 22	−235		Theory	
Ref. 49	−55		OR	*c* plane on Al_2O_3
Ref. 50	−110		OR	*c* plane on Al_2O_3
Ref. 51	−230	(20)	OR	*m*-plane bulk
Ref. 52	−225	36	OR	*a*-/*c*-plane bulk
Ref. 53	−237	(20)	OR	*c* plane on SiC
Ref. 38	−152.4	18.9	CL	*c*-plane heteroepitaxial films
Ref. 54	−206	20	PL	*c* plane on Al_2O_3
Ref. 16	−212	16	SE	*c*-plane heteroepitaxial films
This work (295 K)	-220 ± 2	15 ± 2	SE	*m*-plane bulk
This work (10 K)	-221 ± 2	13 ± 2	SE	*m*-plane bulk

shape decomposition of the ε_2 spectra allows us to identify distinct absorption mechanisms and their energy positions (also shown in Fig. 5). The model is based on Elliot's theory of excitonic absorption[57] and additional contributions taking into account the formation of exciton-phonon complexes (EPCs), as already described in Ref. 16. In detail, the contribution due to excitons is

$$\varepsilon_2^X(\hbar\omega) = \frac{C^X}{(\hbar\omega)^2} \sum_n (\gamma n^3)^{-1} \exp\left(\frac{(\hbar\omega - E)}{\gamma}\right)^2, \quad (3)$$

with $E = E_G - E_B^X/n^2$. Here, E_G is the band-to-band gap, E_B^X is the exciton binding energy, n is the exciton state, and γ is a broadening parameter. C^X represents the corresponding amplitude factor, which is proportional to the oscillator strength. The exciton continuum, also known as

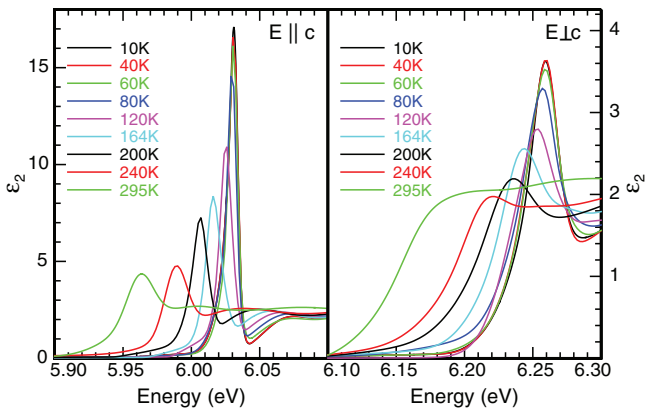

FIG. 4. (Color online) Imaginary parts of (left) the extraordinary and (right) the ordinary dielectric functions as a function of temperature.

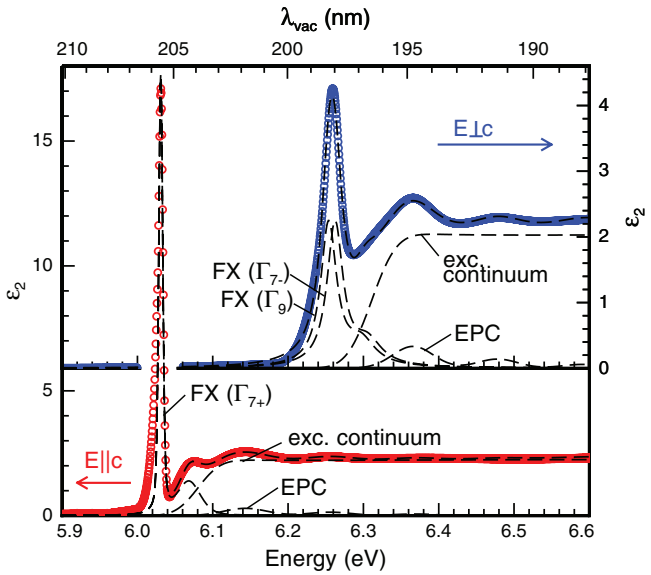

FIG. 5. (Color online) Comparison of experimental (blue and red) and modeled (black) imaginary parts of the dielectric function at $T = 10$ K. The decomposition of the spectra allows us to assign free excitons including excited states (FX), exciton-phonon complexes (EPC), and contributions due to the exciton continuum or band-to-band absorption. The sum of all contributions is also shown and is in good agreement with the experimental data.

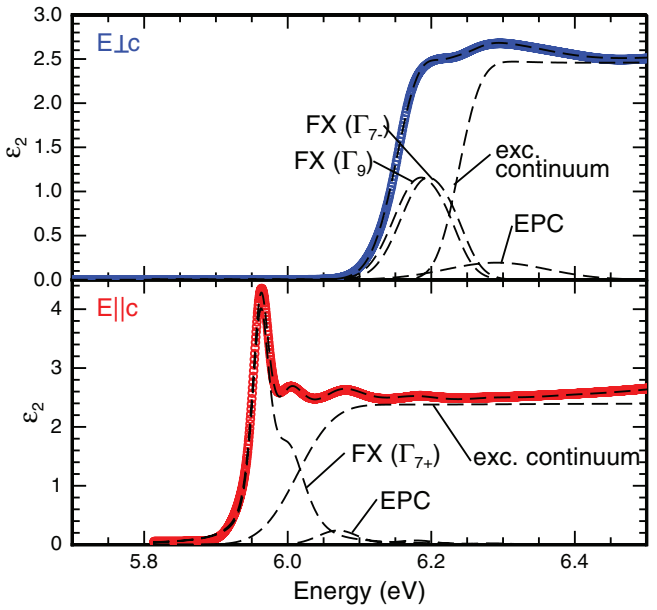

FIG. 6. (Color online) Model fit of the imaginary parts of (top) ordinary and (bottom) extraordinary dielectric functions at room temperature. FX marks a free-exciton transition including excited states with the corresponding valence band symmetry given in brackets. EPC means exciton-phonon coupling, and exc. continuum labels the contributions into the exciton continuum.

Coulomb-enhanced band-to-band transition, is modeled as

$$\varepsilon_2^{BB}(\hbar\omega) = \frac{C^{BB}}{(\hbar\omega)^2} \frac{1 + \mathrm{erf}[(\hbar\omega - E_G)/\gamma)]}{1 - \exp\left[-2\pi^2 \left| E_B^X \right| / (\hbar\omega - E_G)\right]}. \quad (4)$$

Similarly, C^{BB} represents the amplitude, and γ represents the broadening. Finally, the EPCs are described by

$$\varepsilon_2^{EPC}(\hbar\omega) = f_0 \sum_m b^{m-1} \varepsilon_2^X, \quad (5)$$

with E in ε_2^X being replaced by $E = E_G - E_B^X/n^2 + m\hbar\Omega$, where $\hbar\Omega$ is the average contributing LO phonon energy. f_0 and b^{m-1} express the strength of the EPC and its phonon sidebands, respectively.

The same equations [Eqs. (3) to (5)] were used to model ε_2 for both electric field polarizations at all experimentally investigated temperatures. The highest accessible temperature was room temperature ($T = 295$ K) in our case, where all the features suffer the maximum broadening and damping due to phonons. However, excitonic resonances, their excited states, EPCs, and the exciton continuum are still clearly resolvable, as shown in Fig. 6.

The characteristic energy values obtained from the modeling are summarized in Table IV. The anisotropy is found to be nearly independent of the temperature. The same is true for the exciton binding energies and the average phonon energies of the EPC. The observed small decrease in phonon energy of the longitudinal optical phonons is in line with earlier published experimental studies.[58] However, absolute energy positions of all contributions shift to lower energies when the temperature is increased, which is expected due to thermal expansion and the electron-phonon interaction. The energy shift from 10 to 295 K amounts to 70 meV for the extraordinary DF, in agreement with earlier studies,[16,55] and 71 and 72 meV for the ordinary DF.

TABLE IV. Characteristic energy values (in eV) extracted by model fitting to the experimentally obtained imaginary parts of the dielectric functions at 10 and 295 K. The accuracy of absolute energy positions from ellipsometry is ±1 meV.

		T (K)	
	Parameter	10	295
E ∥ **c**	FX(Γ_{7+})	6.032	5.962
	$E_{X,b}$	0.053	0.050
	$\hbar\Omega_{LO}$	0.110	0.108
E ⊥ **c**	FX(Γ_9)	6.255	6.183
	FX(Γ_{7-})	6.264	6.193
	$E_{X,b}$	0.055	0.052
	$\hbar\Omega_{LO}$	0.111	0.109

From the energy values reported in Table IV we calculated[16] a crystal-field splitting of $\Delta_{cf} = (-221 \pm 2)$ meV (-220 meV) and a spin-orbit energy of $\Delta_{so} = (13 \pm 2)$ meV (15 meV) for low (room) temperature. For these calculations we took into account that the observed Γ_{7+} exciton resonance energy corresponds to the Γ_1 exciton symmetry, and the degenerate Γ_{7+} energy position is $-3j/2 = 6$ meV higher in energy.[14] The value for $j = -4$ meV is taken to be independent of the temperature, while values of Γ_9 and Γ_{7-} excitons are used without further corrections. The values for Δ_{cf} and Δ_{so} are only slightly different from our previously reported parameter set based on thin epitaxial c-plane layers analyzed at room temperature.[16] However, due to the unrivaled quality of the sample under study here, visible, e.g., because of the intense and sharp excitonic resonances and the correction for spin-exchange interaction of the A transition, we consider the current values to be more reliable for unstrained AlN with low point-defect density.

D. Emission properties

Now we correlate the absorption features around the band gap with the emission properties. PL spectra of the near-band-gap energy region recorded from the same sample are shown in Fig. 7. We observe the same general redshift with increasing temperature as in ellipsometry assigned to exciton contributions formed with holes from the highest (Γ_{7+}) VB. We detect no luminescence from the higher transition energies located around 6.2 eV due to the fact that in our temperature regime the corresponding VBs are almost not populated.

A detailed analysis of the PL spectra allows for an assignment of the two dominating bands at low temperature to donor bound-exciton contributions D^0X. They peak at 6.0073 ± 0.0003 and 6.0132 ± 0.0003 eV. While the low-energy one is not identified yet, the latter one is assigned to excitons bound to the shallow neutral-donor silicon. At their high-energy shoulder, we observe two broader bands stemming from free-exciton recombinations with holes from the highest VB, which we label Γ_1 and Γ_5 according to their symmetry. With increasing temperature these bands quench slower than the D^0X lines due to their successive thermal

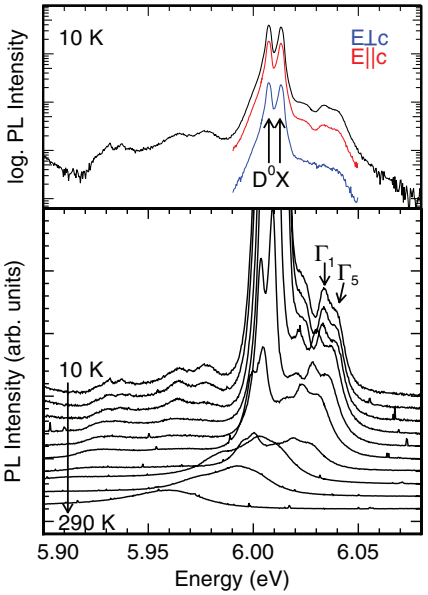

FIG. 7. (Color online) (bottom) Selected photoluminescence spectra for different temperatures ($T = 10$, 25, 44, 78, 98, 124, 150, 200, 230, 290 K). The high-intensity part is cut, and the spectra are shifted for clarity. Γ_1 and Γ_5 label the radiative bands assigned to free excitons formed with holes from the Γ_{7+} valence band and mark their symmetry, respectively. (top) Logarithmic plot of the spectrum at $T = 10$ K. Two similarly intense donor bound excitons D^0X dominate the spectrum. Bound- and free-exciton spectra for different polarization directions of the electric field are shown in red ($\mathbf{E} \parallel \mathbf{c}$, stronger spectrum) and blue ($\mathbf{E} \perp \mathbf{c}$, weaker spectrum), respectively.

dissociation. The free-exciton bands have their maxima at 6.032 ± 0.0005 and 6.040 ± 0.0005 eV (at $T = 10$ K), respectively. The contribution at 6.032 eV could be assigned to excitons having Γ_1 symmetry; the higher-energy component at 6.040 eV is assigned to excitons with Γ_5 symmetry. The former are also visible in the DF at the same energy value, while the latter remains too weak for detection by SE.[14] This fact is consistent with perturbation theoretical calculations. When calculating the relative oscillator strengths of the Γ_1 and Γ_5 excitons by using a 12×12 **kp** Hamiltonian[59] and setting the spin-exchange interaction to $j = -4$ meV,[14] we find that the Γ_1 exciton has a very strong oscillator strength (close to 1) for $E \parallel c$, but it is zero for $\mathbf{E} \perp \mathbf{c}$. In contrast, the Γ_5 exciton has an oscillator strength of zero for $\mathbf{E} \parallel \mathbf{c}$ and only around 4×10^{-4} for $\mathbf{E} \perp \mathbf{c}$. These results are in perfect agreement with our experimental findings, as Γ_5 excitons can only show up in nonequilibrium experiments (luminescence) if $\mathbf{E} \perp \mathbf{c}$ is probed.

In Fig. 8 we collect the energy values for the free-exciton recombination and absorption bands, as observed in PL and SE as a function of temperature. The agreement between the values from both techniques is obvious; i.e., the free exciton visible in SE falls onto the lower-energy exciton state observed in PL. Additionally, in Fig. 8 we present model fits to the temperature evolution of the energy position of all three excitons as measured by SE using the model developed by Pässler.[60] The obtained best fit parameters are given in the figure.

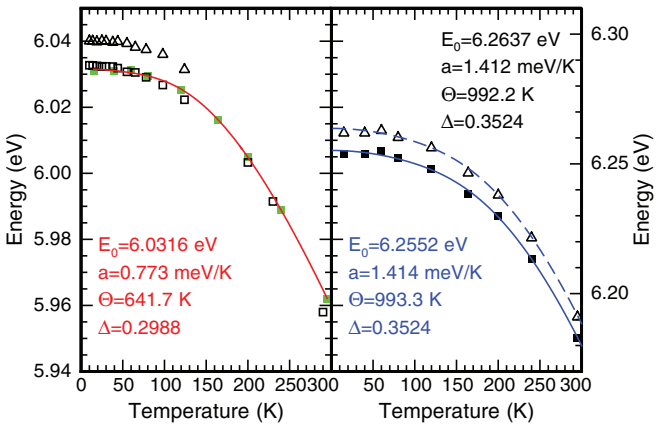

FIG. 8. (Color online) Temperature-dependent positions of free excitons (symbols) and corresponding Pässler fits (solid and dashed lines). The Pässler parameters are given. In the left graph the green solid squares are resonance energy positions obtained by ellipsometry, and the open symbols are peak energies as read from PL spectra. In the right graph all experimental data points were taken from ellipsometry.

It is very interesting to directly compare the spectra recorded by different optical techniques. An overview is given in Fig. 9, where we compare data at $T = 10$ K. The DFs were used to calculate an unpolarized reflectivity for normal-incidence light,[61] which is in turn compared to experimental data measured with a D_2 lamp as an unpolarized light source under normal incidence and with synchrotron radiation under slanted incidence of light. The PL spectrum and a PLE spectrum (using a weak low-energy defect luminescence band as a monitor) are displayed as well. It is found that the position of the Γ_1-symmetry free exciton with a hole of the A VB matches perfectly with the dip in the PLE spectrum. We assign this behavior to enhanced exciton generation at

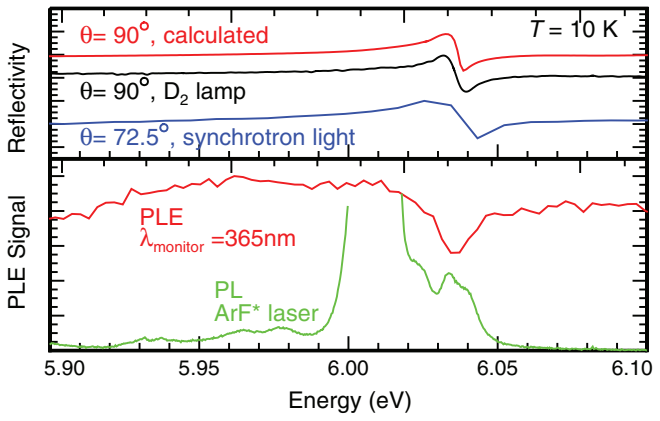

FIG. 9. (Color online) The bottom graph compares a photoluminescence excitation spectrum (red, top trace) with photoluminescence (green, bottom trace). The bound excitons of the PL spectrum are cut for clarity. The top graph shows shifted reflectivity spectra measured by synchrotron radiation under tilted incidence (blue, bottom trace) and by a deuterium lamp under nearly perpendicular incidence using unpolarized light (black, middle trace). Additionally, a calculated reflectivity spectrum for the same conditions is shown (red, top trace). All data are recorded at 10 K.

resonance energy. Note that these excitons do not easily transform into the defect luminescence we detect here, which is therefore of nonexcitonic nature. Obviously, techniques presented here complement each other and thus yield well-founded assignments and interpretations.

IV. SUMMARY AND CONCLUSIONS

We have presented and analyzed the ordinary and extraordinary DFs of a high-quality nonpolar bulk AlN singly crystalline sample from 0.58 up to 20 eV at room temperature. High-energy features were evaluated, labeled, and assigned after comparison with spectra of GaN and theoretical results. The low-energy dispersion of ε_1 yields the high-frequency dielectric constants $\varepsilon_{\infty\perp} = 4.14 \pm 0.02$ and $\varepsilon_{\infty\parallel} = 4.34 \pm 0.02$, from which the static ones are calculated to be $\varepsilon_{S\perp} = 7.65$ and $\varepsilon_{S\parallel} = 9.21$. The DFs around the band gap were analyzed in greater detail as a function of temperature between 10 and 295 K. The anisotropy of the different detected exciton states yields a crystal-field energy of $\Delta_{cf} = (221 \pm 2)$ meV and a spin-orbit splitting of $\Delta_{so} = (13 \pm 2)$ meV at low temperature. These results were compared to earlier reported values from the literature. Furthermore, a detailed decomposition and modeling of the DFs around the band gap energy yield evidence for participation of exciton-phonon complexes, excited excitonic states, and band-to-band transitions in the overall absorption. The free-exciton energies were analyzed as a function of temperature and are compared to photoluminescence spectra also recorded at variable temperature. Both techniques show a nearly perfect agreement as a function of temperature. This behavior could be described successfully by the Pässler model. At low temperature, we furthermore showed reflectivity spectra obtained in different setups and geometries and a calculated reflectivity curve and compared them to photoluminescence and photoluminescence excitation spectra, further supporting our assignments.

Note added in Proof: Very recently a further study dealing with spin-exchange interaction in AlN has been published (Ref. 62). There, the spin-exchange interaction constant was found to be $j = +6.8$ meV unlike our $j = -4$ meV. The opposite sign of j in Ref. 62 is related to a different assignment of exciton transitions resulting in a reversed energy order of free excitons compared to our work. However, the relative oscillator strengths of Γ_1 and Γ_5 excitons calculated by either value of j remains virtually unchanged to our present results.

ACKNOWLEDGMENTS

Part of this work was funded by the Deutsche Forschungsgemeinschaft DFG in the framework of Major Research Instrumentation Program No. INST 272/205-1, which we gratefully acknowledge. Furthermore, we gratefully acknowledge support by the synchrotron radiation sources BESSY II of Helmholtz-Zentrum Berlin (HZB) and DORIS III at DESY, Hamburg (both in Germany). DESY is a member of the Helmholtz Association (HGF). We would like to thank A. Kotlov for excellent assistance in using beamline I at DESY. ISAS was supported by the Federal State of Berlin within EFRE Project No. 20072013 2/41. Part of this work was supported by the EU within the 7th RTD Framework (project RAINBOW: Contract No. PITN-GA-2008-213238).

*Corresponding author: martin.feneberg@ovgu.de

†Present address: Leibniz Institute for Crystal Growth, Max-Born-Strasse 2, 12489 Berlin, Germany.

[1] Y. Taniyasu, M. Kasu, and T. Makimoto, Nature (London) **441**, 325 (2006).

[2] M. Bickermann, B. M. Epelbaum, O. Filip, P. Heimann, S. Nagata, and A. Winnacker, Phys. Status Solidi C **7**, 21 (2010).

[3] R. Collazo, J. Xie, B. E. Gaddy, Z. Bryan, R. Kirste, M. Hoffmann, R. Dalmau, B. Moody, Y. Kumagai, T. Nagashima, Y. Kubota, T. Kinoshita, A. Koukitu, D. L. Irving, and Z. Sitar, Appl. Phys. Lett. **100**, 191914 (2012).

[4] T. Nishida, T. Makimoto, H. Saito, and T. Ban, Appl. Phys. Lett. **84**, 1002 (2004).

[5] Z. Ren, Q. Sun, S.-Y. Kwon, J. Han, K. Davitt, Y. K. Song, A. V. Nurmikko, H.-K. Cho, W. Liu, J. A. Smart, and L. J. Schowalter, Appl. Phys. Lett. **91**, 051116 (2007).

[6] M. Kneissl, Z. Yang, M. Teepe, C. Knollenberg, O. Schmidt, P. Kiesel, N. M. Johnson, S. Schujman, and L. J. Schowalter, J. Appl. Phys. **101**, 123103 (2007).

[7] T. Wunderer, C. L. Chua, Z. Yang, J. E. Northrup, N. M. Johnson, G. A. Garrett, H. Shen, and M. Wraback, Appl. Phys. Express **4**, 092101 (2011).

[8] B. M. Epelbaum, C. Seitz, A. Magerl, M. Bickermann, and A. Winnacker, J. Cryst. Growth **265**, 577 (2004).

[9] E. N. Mokhov, O. V. Avdeev, I. S. Barash, T. Yu. Chemekova, A. D. Roenkov, A. S. Segal, A. A. Wolfson, Yu. N. Makarov, M. G. Ramm, and H. Helava, J. Cryst. Growth **281**, 93 (2005).

[10] Z. G. Herro, D. Zhuang, R. Schlesser, R. Collazo, and Z. Sitar, J. Cryst. Growth **286**, 205 (2006).

[11] M. Feneberg, B. Neuschl, K. Thonke, R. Collazo, A. Rice, Z. Sitar, R. Dalmau, J. Xie, S. Mita, and R. Goldhahn, Phys. Status Solidi A **208**, 1520 (2011).

[12] B. Neuschl, K. Thonke, M. Feneberg, S. Mita, A. Xie, R. Dalmau, R. Collazo, and Z. Sitar, Phys. Status Solidi B **249**, 511 (2012).

[13] M. Funato, K. Matsuda, R. G. Banal, R. Ishii, and Y. Kawakami, Phys. Rev. B **87**, 041306 (2013).

[14] M. Feneberg, M. F. Romero, B. Neuschl, K. Thonke, M. Röppischer, C. Cobet, N. Esser, M. Bickermann, and R. Goldhahn, Appl. Phys. Lett. **102**, 052112 (2013).

[15] G. Rossbach, M. Röppischer, P. Schley, G. Gobsch, C. Werner, C. Cobet, N. Esser, A. Dadgar, M. Wieneke, A. Krost, and R. Goldhahn, Phys. Status Solidi B **247**, 1679 (2010).

[16] G. Rossbach, M. Feneberg, M. Röppischer, C. Werner, N. Esser, C. Cobet, T. Meisch, K. Thonke, A. Dadgar, J. Bläsing, A. Krost, and R. Goldhahn, Phys. Rev. B **83**, 195202 (2011).

[17]C. Persson, R. Ahuja, A. Ferreira da Silva, and B. Johansson, J. Cryst. Growth **231**, 407 (2001).
[18]F. Bechstedt, K. Seino, P. H. Hahn, and W. G. Schmidt, Phys. Rev. B **72**, 245114 (2005).
[19]L. C. de Carvalho, A. Schleife, and F. Bechstedt, Phys. Rev. B **84**, 195105 (2011).
[20]S. Sharma, J. K. Dewhurst, A. Sanna, and E. K. U. Gross, Phys. Rev. Lett. **107**, 186401 (2011).
[21]R. Laskowski and N. E. Christensen, Phys. Rev. B **74**, 075203 (2006).
[22]A. Riefer, F. Fuchs, C. Rödl, A. Schleife, F. Bechstedt, and R. Goldhahn, Phys. Rev. B **84**, 075218 (2011).
[23]L. X. Benedict, T. Wethkamp, K. Wilmers, C. Cobet, N. Esser, E. L. Shirley, W. Richter, and M. Cardona, Solid State Commun. **112**, 129 (1999).
[24]P. Schley, J. Räthel, E. Sakalauskas, G. Gobsch, M. Wieneke, J. Bläsing, A. Krost, G. Koblmüller, J. S. Speck, and R. Goldhahn, Phys. Status Solidi A **207**, 1062 (2010).
[25]C. Cobet, R. Goldhahn, W. Richter, and N. Esser, Phys. Status Solidi B **246**, 1440 (2009).
[26]R. Goldhahn, Acta Phys. Pol. A **104**, 123 (2003).
[27]G. Zimmerer, Radiat. Meas. **42**, 859 (2007).
[28]C. Buchheim, R. Goldhahn, M. Rakel, C. Cobet, N. Esser, U. Rossow, D. Fuhrmann, and A. Hangleiter, Phys. Status Solidi B **242**, 2610 (2005).
[29]P. Y. Yu and M. Cardona, *Fundamentals of Semiconductor Physics and Materials Properties*, 4th ed. (Springer, Berlin, 2010), p. 253.
[30]P. Schley, R. Goldhahn, A. T. Winzer, G. Gobsch, V. Cimalla, O. Ambacher, H. Lu, W. J. Schaff, M. Kurouchi, Y. Nanishi, M. Rakel, C. Cobet, and N. Esser, Phys. Rev. B **75**, 205204 (2007).
[31]D. E. Aspnes, Phys. Rev. Lett. **28**, 168 (1972).
[32]The name high-frequency dielectric constant and thus the label ε_∞ stem from the analysis of infrared spectra where all contributions to the DF from interband transitions are taken into account by ε_∞. When analyzing data in the ultraviolet and visible spectral range, ε_∞ yields the asymptotic value for very low frequencies, assuming no further phononic or plasmonic contributions. The limit for high photon energy is in any case 1. In principle, ε_∞ as used here thus allows a connection of ultraviolet and infrared spectra.
[33]B. Gil, Phys. Rev. B **81**, 205201 (2010).
[34]B. Gil, B. Guizal, D. Felbacq, and B. Bouchitté, Eur. Phys. J. Appl. Phys. **53**, 20303 (2011).
[35]S. Shokhovets, R. Goldhahn, G. Gobsch, S. Piekh, R. Lantier, A. Rizzi, V. Lebedev, and W. Richter, J. Appl. Phys. **94**, 307 (2003).
[36]R. H. Lyddane, R. G. Sachs, and E. Teller, Phys. Rev. **59**, 673 (1941).
[37]V. Yu. Davydov, Yu. E. Kitaev, I. N. Goncharuk, A. N. Smirnov, J. Graul, O. Semchinova, D. Uffmann, M. B. Smirnov, A. P. Mirgorodsky, and R. A. Evarestov, Phys. Rev. B **58**, 12899 (1998).
[38]H. Ikeda *et al.*, J. Appl. Phys. **102**, 123707 (2007).
[39]A. Rubio, J. L. Corkill, M. L. Cohen, E. L. Shirley, and S. G. Louie, Phys. Rev. B **48**, 11810 (1993).
[40]M. Suzuki, T. Uenoyama, and A. Yanase, Phys. Rev. B **52**, 8132 (1995).
[41]S.-H. Wei and A. Zunger, Appl. Phys. Lett. **69**, 2719 (1996).
[42]K. Kim, W. R. L. Lambrecht, B. Segall, and M. van Schilfgaarde, Phys. Rev. B **56**, 7363 (1997).
[43]K. Shimada, T. Sota, and K. Suzuki, J. Appl. Phys. **84**, 4951 (1998).
[44]S. K. Pugh, D. J. Dugdale, S. Brand, and R. A. Abram, Semicond. Sci. Technol. **14**, 23 (1999).
[45]J. M. Wagner and F. Bechstedt, Phys. Rev. B **66**, 115202 (2002).
[46]J. Li, K. B. Nam, M. L. Nakarmi, J. Y. Lin, H. X. Jiang, P. Carrier, and S.-H. Wei, Appl. Phys. Lett. **83**, 5163 (2003).
[47]P. Carrier and S.-H. Wei, J. Appl. Phys. **97**, 033707 (2005).
[48]L. C. de Carvalho, A. Schleife, F. Fuchs, and F. Bechstedt, Appl. Phys. Lett. **97**, 232101 (2010).
[49]T. Onuma, S. F. Chichibu, T. Sota, K. Asai, S. Sumiya, T. Shibata, and M. Tanaka, Appl. Phys. Lett. **81**, 651 (2002).
[50]J. Chen, W. Z. Shen, H. Ogawa, and Q. X. Guo, Appl. Phys. Lett. **84**, 4866 (2004).
[51]L. Chen, B. J. Skromme, R. F. Dalmau, R. Schlesser, Z. Sitar, C. Chen, W. Sun, J. Yang, M. A. Khan, M. L. Nakarmi, J. Y. Lin, and H.-X. Jiang, Appl. Phys. Lett. **85**, 4334 (2004).
[52]E. Silveira, J. A. Freitas, O. J. Glembocki, G. A. Slack, and L. J. Schowalter, Phys. Rev. B **71**, 041201(R) (2005).
[53]G. M. Prinz, A. Ladenburger, M. Schirra, M. Feneberg, K. Thonke, R. Sauer, Y. Taniyasu, M. Kasu, and T. Makimoto, J. Appl. Phys. **101**, 023511 (2007).
[54]A. Sedhain, J. Y. Lin, and H. X. Jiang, Appl. Phys. Lett. **92**, 041114 (2008).
[55]M. Feneberg, R. A. R. Leute, B. Neuschl, K. Thonke, and M. Bickermann, Phys. Rev. B **82**, 075208 (2010).
[56]R. A. R. Leute, M. Feneberg, R. Sauer, K. Thonke, S. B. Thapa, F. Scholz, Y. Taniyasu, and M. Kasu, Appl. Phys. Lett. **95**, 031903 (2009).
[57]R. Elliot, Phys. Rev. **108**, 1384 (1957).
[58]J. M. Hayes, M. Kuball, Y. Shi, and J. H. Edgar, Jpn. J. Appl. Phys. **39**, L710 (2000).
[59]R. Ishii, A. Kaneta, M. Funato, Y. Kawakami, and A. A. Yamaguchi, Phys. Rev. B **81**, 155202 (2010).
[60]R. Pässler, Phys. Rev. B **66**, 085201 (2002).
[61]M. Feneberg, M. Röppischer, C. Cobet, N. Esser, B. Neuschl, T. Meisch, K. Thonke, and R. Goldhahn, Appl. Phys. Lett. **99**, 021903 (2011).
[62]R. Ishii, M. Funato, and Y. Kawakami, Phys. Rev. B **87**, 161204(R) (2013).